



Contents lists available at ScienceDirect

Arabian Journal of Chemistry

journal homepage: www.ksu.edu.sa

Original article

Chitosan/magnetic biochar composite with enhanced reusability: Synergistic effect of functional groups and multilayer structure

Yongbo Yu^{a,b}, Wanting Liu^{a,b}, Yinuo Zhang^a, Bolun Zhang^{a,b}, Yiping Jin^{a,b}, Siji Chen^{a,b}, Shanshan Tang^{a,b,*}, Yingjie Su^{a,b}, Xiaoxiao Yu^{a,b}, Guang Chen^{a,b}

^a College of Life Sciences, Jilin Agricultural University, Changchun 130118, China

^b Key Laboratory of Straw Comprehensive Utilization and Black Soil Conservation, Ministry of Education, Jilin Agricultural University, Changchun 130118, China



ARTICLE INFO

Keywords:

Chitosan
Magnetic biochar
Crosslinking
Cr(VI) removal
Reusability

ABSTRACT

Heavy metals in water bodies pose a significant threat to both ecology and human well-being. Therefore, the development of green and sustainable adsorbents for water remediation is essential. This study presents a crosslinked chitosan composite structure with multiple layers, which was generated by adjusting the ratio of chitosan to wheat straw-derived magnetic biochar in the composite. The adsorption behavior of the composite under different conditions was revealed by varying the Cr(VI) concentration, pH, and temperature. The composite exhibited a maximum adsorption of 121.8 mg g⁻¹ for Cr(VI) in water, which was 11.9 times higher than that of magnetic biochar. It maintained a residual performance of 78.6 % after seven cycles, higher than most chitosan-based composites. The reusability was improved via hydrochloric acid protonation of functional groups and layer-by-layer exposure of the composite structure. This study provides new insights into the application of composites derived from chitosan and wheat straw, an agricultural waste, as sustainable adsorbents.

1. Introduction

Water is an invaluable resource for human survival, with water quality playing a pivotal role in both domestic and industrial applications. Three major properties of water that support its release of heavy metals and other hazardous waste into water bodies as mentioned by Cao et al. (2022), Saleem et al. (2022), and Wang et al. (2023b) are solubility, polar nature, buoyancy and density. In particular, chromium (Cr), with Cr(VI) being the more perilous form due to its high solubility and bioavailability, is extensively discharged into water environments during various industrial activities, including metallurgy, tannery operations, and electroplating (Xu et al., 2019; Chin et al., 2022; Zhao et al., 2022). Prolonged exposure to heavy metals has been associated with adverse effects on the human body, including skin dermatitis, liver and kidney damage, and hair loss. Hence, the elimination of Cr(VI) from wastewater is of critical importance (Langård and Costa, 2015). However, conventional removal methods are costly and inefficient; therefore, the development of a cost-effective, efficient, easily recoverable, and reusable adsorbent has become a new challenge.

Current approaches for extracting heavy metals from water mainly consist of biological treatment (Zhu et al., 2022), advanced oxidation

techniques (Ma et al., 2020), chemical precipitation (Grimshaw et al., 2011), membrane separation (Teng et al., 2023), and adsorption (Islam et al., 2023), among which the latter offers many adsorption has a number of advantages, including cost-effectiveness, efficiency, and ease of operation (Wang et al., 2023a). Biochar, a solid substance formed by the pyrolysis of biomass under anaerobic or anoxic conditions, can be used as an adsorbent to eliminate pollutants from wastewater based on the diffusion of pollutants into the pores of biochar, where they are effectively fixed through physical and chemical interactions (Zhang et al., 2022a; Wang et al., 2020). Moreover, the surface functional groups of biochar can effectively remove heavy metals from water and transform them into less bioavailable forms via chelation, precipitation, chemisorption, and conversion mechanisms. Straw is a promising precursor for producing biochar because it is inexpensive, widely sourced, and nontoxic. However, the powdered nature of straw-derived biochar poses challenges in terms of recycling. To circumvent this issue, magnetic modification of straw-derived biochar stands out as a promising approach. Magnetic materials have various applications in environmental remediation, such as the recovery of adsorbents, and in biomedicine, such as the immobilization of proteins. This is due to their superparamagnetic properties, high magnetization, high

* Corresponding author at: College of Life Sciences, Jilin Agricultural University, Changchun 130118, China.

E-mail address: tangshanshan81@163.com (S. Tang).

<https://doi.org/10.1016/j.arabjc.2024.105746>

Received 30 January 2024; Accepted 19 March 2024

Available online 20 March 2024

1878-5352/© 2024 The Authors. Published by Elsevier B.V. on behalf of King Saud University. This is an open access article under the CC BY-NC-ND license (<http://creativecommons.org/licenses/by-nc-nd/4.0/>).

biocompatibility, and unique physicochemical properties. Among the various magnetic materials, Fe_3O_4 magnetic particles are widely used because of their small size and low toxicity (Wang et al., 2023c). The combination of biochar and Fe_3O_4 enhances the magnetic selectivity and facilitates the separation of solid and liquid phases. Nevertheless, simple Fe_3O_4 magnetic particles tend to aggregate, leading to poor stability and scarcity of functional groups (Zhao et al., 2023). The aggregation of magnetic particles can be prevented by loading them onto the biochar surface as a uniform dispersion, which also exposes more active centers (Wu et al., 2022). There exist various methods for loading magnetic particles, such as calcination (Mo et al., 2020), co-precipitation (An et al., 2022), and liquid phase reduction methods (Zhao et al., 2020). However, many of these methods require multiple preparation processes and expensive raw materials. Moreover, the magnetic particles easily shed from the material. Therefore, there is a need to design a rational structure to encapsulate the magnetic particles and reduce their loss during the reuse process.

Chitosan, also known as deacetylated chitin, is a nontoxic, renewable, and biodegradable biopolymer derived from natural sources (Lee et al., 2023). The presence of abundant amino and hydroxyl groups in chitosan enables its effective complexation and coordination with heavy metals and composite biochar (Chen et al., 2019). However, the use of chitosan is constrained by its inadequate mechanical robustness, instability, and challenges associated with water-based recycling. Chitosan has been used to crosslink the biochar surface, thus obtaining additional adsorption sites with good stability (Gao et al., 2022). However, the limited reusability of the material hinders its practical application. The adsorption capacity decreases dramatically with the depletion of active sites. In addition, during the regeneration process of the adsorbent, the eluent may cause further shedding of the active material on the surface. Therefore, it is essential to develop a strategy to reduce the loss of active sites on the material surface. Moreover, many chitosan-based composites involve expensive raw materials with complex preparation processes. In this context, we were interested in investigating the preparation of chitosan-based composites using wheat straw, an economical raw material that is expected to meet or even exceed the performance of existing adsorbents. To the best of our knowledge, the synthesis of chitosan-based composite adsorbents using wheat straw has not been reported.

The design of specific material structures for diverse applications attracts considerable research attention. For example, nanostructures can effectively promote good ion transport properties (Yedluri and Kim, 2019), two-dimensional porous structures contribute to achieve good mechanical stability and electrochemical activity (Kumar et al., 2023a), and two-phase crystalline materials with near-spherical structures help reduce the impedance between the material interface and the electrolyte solution (Ramachandran et al., 2023b). Most of the studies confirm that the rational design of the structure of the material has a non-negligible positive enhancement of the material properties (Anil Kumar and Kim, 2018a). Consequently, designing a material that can provide efficient pollutant removal performance in terms of reusability and effectively retain the active sites during adsorption has become a major challenge for water management. Several studies have inspired us to synthesis of specific structures by adjusting the proportions of the phases in a composite (Anil Kumar et al., 2020; Hegazy et al., 2023; Ramachandran et al., 2023a).

Herein, we synthesized a composite material (MWSBC-C) consisting of wheat straw-derived magnetic biochar and chitosan. It was used as an adsorbent for the removal of Cr(IV) from water. Wheat straw, being one of the agricultural wastes with huge production, is a very attractive solution as a carbon precursor for magnetic biochar in order to enhance its added value. By adjusting the optimal ratio of chitosan to magnetic biochar, a stable and dense cross-linking structure unique to MWSBC-C was successfully constructed, which significantly improved its adsorbent regeneration performance. The materials were characterized and subjected to batch adsorption experiments using various tools to determine

the role and mechanism of their structural and functional group properties in the adsorption process. We hope that wheat straw can be a potentially economical option for the preparation of efficient and sustainable green adsorbents. In addition, this study aims to provide a theoretical basis for improving the performance of chitosan-based composites during reuse.

2. Experimental section

2.1. Materials and chemicals

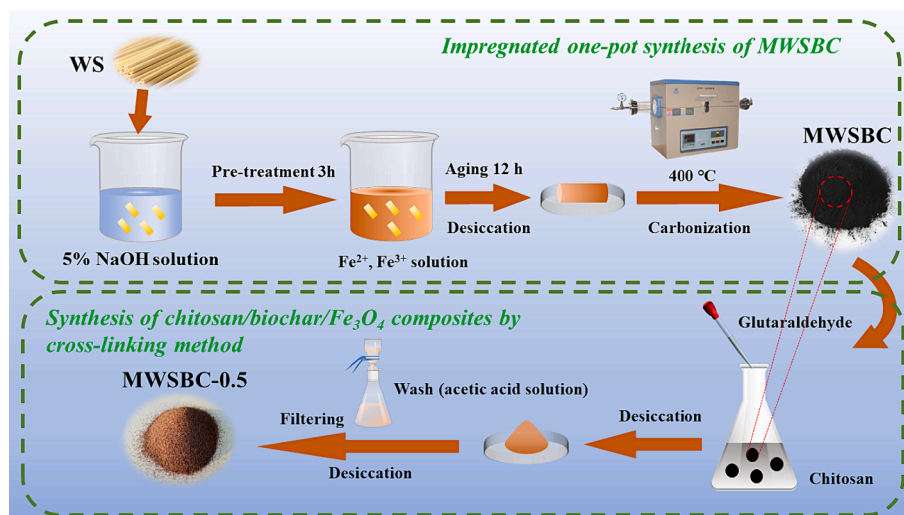
Wheat straw (WS) was acquired from Changchun, Jilin Province, China. All reagents were of analytical grade and required no further purification (Yedluri and Kim, 2018; Kumar et al., 2024b; Anil Kumar and Kim, 2018b). Adsorption experiments, washing, and sample preparation were conducted using deionized water obtained in the laboratory. A real water sample with a temperature of 291 K was extracted from a lake at Jilin Agricultural University in China.

2.2. Preparation of magnetic biochar by one-pot impregnation method

The WS sample was cleaned and dried at 333 K for 48 h and then finely crushed and sifted through a 60-mesh sieve. To enhance the impregnation effect, WS was subjected to alkaline pretreatment by immersing 10 g of WS in 1 L of a 5 % NaOH solution followed by magnetic stirring for 3 h. Then, the pretreated WS sample was thoroughly rinsed with water and immersed in a solution comprising 300 mL of $\text{FeSO}_4 \cdot 7\text{H}_2\text{O}$ with a concentration of 0.25 mol/L and $\text{FeCl}_3 \cdot 6\text{H}_2\text{O}$ with a concentration of 0.5 mol/L (molar ratio of 1:2) (Huang et al., 2021). After adjusting the pH to 10, the system was subjected to ultrasonic treatment for 20 min and left to age for 12 h. The resulting sample was washed until neutral and dried at 333 K for 48 h. Subsequently, the sample was heated in a nitrogen-protected horizontal tube furnace, at a heating rate of 10 K min^{-1} and maintained at 673 K for 2 h. After cooling to room temperature, the sample was ground and washed with deionized water to remove soluble carbonates. The obtained sample was denoted as MWSBC. For comparison, another biochar sample, which was denoted as WSBC, was prepared by heating WS at 673 K for 2 h under a nitrogen atmosphere.

2.3. Preparation of the chitosan/biochar/ Fe_3O_4 composite

The chitosan loading was conducted using the crosslinking method with glutaraldehyde as the crosslinking agent (Scheme 1). In brief, 0.5 g of chitosan was dissolved in 33 mL (2.0 wt%) of acetic acid solution under mechanical stirring until all air bubbles disappeared. To this chitosan solution, 15 mg of MWSBC was added. The mixture was then sonicated for 20 min before adding 466 μL (25 wt%) of glutaraldehyde dropwise. Strong stirring at 313 K for 3 h was performed, followed by drying at 333 K for 12 h. Excess chitosan was removed by repeatedly washing with 2 wt% acetic acid solution and deionized water, and a final drying at 333 K for 24 h was performed. The resulting product was crushed and ready for use. Samples of magnetic biochar of chitosan with different chitosan dosages (0.25, 0.5, 0.75, and 1 g) were denoted as MWSBC-C, where C represents the chitosan dosage. For comparison, a WSBC-loaded chitosan sample (WSBC-C) and Fe_3O_4 nanoparticles loaded with chitosan ($\text{Fe}_3\text{O}_4\text{-C}$) were prepared. The loading conditions of WSBC and MWSBC were optimized on the basis of the chitosan dosage. The results are depicted in Fig. S1 (Supporting Information). Considering that increasing the amount of chitosan beyond 0.5 g did not significantly enhance the performance of MWSBC-C in Cr(VI) removal, 0.5 g was selected as the optimal condition for subsequent characterization and adsorption experiments for cost-saving reasons.



Scheme 1. Schematic diagram of the preparation process of MWSBC-0.5.

2.4. Characterization and adsorption experiments

More details of the characterization and adsorption experiments are available in the [Supporting Information](#).

3. Results and discussion

3.1. Sample characterization

To enhance comprehension of the surface morphology and chemical composition of MWSBC-0.5, a series of characterizations were conducted. The microscopic morphology of the samples after loading chitosan was observed via scanning electron microscopy (SEM), and the results are shown in Fig. 1. As demonstrated in Fig. 1a and 1b, the surface of biochar displayed a coarse fibrous structure and formed uneven folds resembling snowflakes, indicating its amorphous carbon nature. This characteristic can be attributed to the high-temperature

carbonization process. In contrast, after the incorporation of chitosan and magnetic particles, some changes were observed in the amorphous structure of WSBC, with certain parts appearing smoother (Fig. 1c and 1d), indicating that a dense chitosan structure was formed via cross-linking. Transmission electron microscopy revealed MWSBC with Fe_3O_4 nanoparticles with distinct edges to the peripheral chitosan (Fig. S2, Supporting Information) (Ramachandran et al., 2023c; Kumar et al., 2023b). Furthermore, the diffraction signals in the selected area electron diffraction pattern are weakened owing to the chitosan coating, although the crystal surface remains clearly identifiable. (Kumar et al., 2023b). The elemental composition of the WSBC and MWSBC-0.5 was analyzed using energy dispersive spectroscopy (EDS) as shown in Fig. S3 and Table S1 (Supporting Information). According to the EDS data, MWSBC-0.5 exhibited a higher proportion of N, Fe, and O elements compared with WSBC. This suggests that the presence of magnetic particles and chitosan not only conferred magnetic properties to the material but also introduced additional N and Fe elements (Qu et al.,

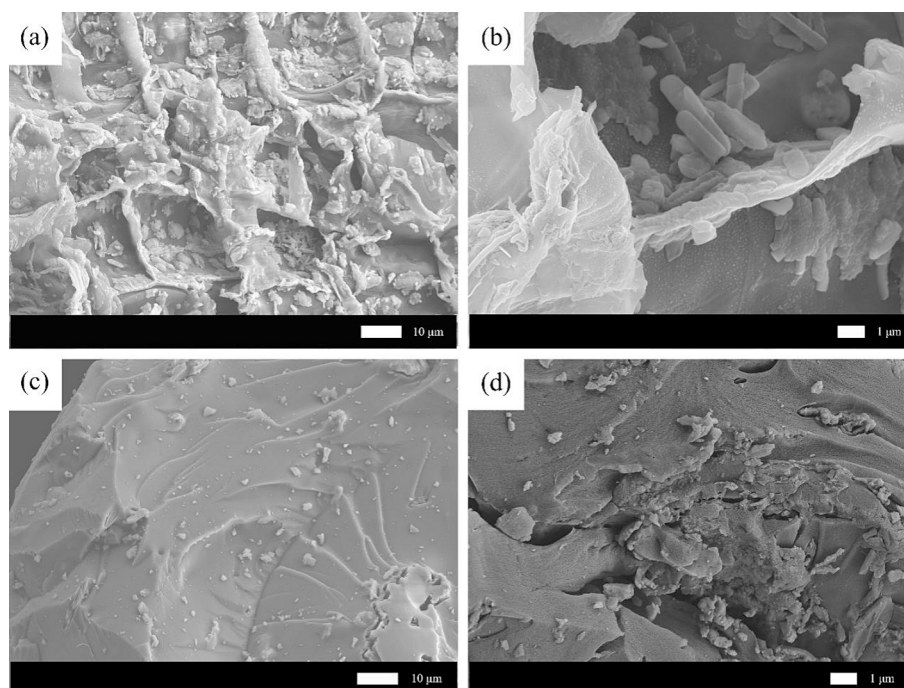


Fig. 1. SEM images of WSBC (a and b), MWSBC-0.5 (c and d).

2022).

The specific surface area (SSA) and porosity of the samples were analyzed, and the resulting data are provided in Table S2 (Supporting Information). The SSA of MWSBC ($3.01 \text{ m}^2 \text{ g}^{-1}$) obtained via a one-step process was lower than that of WSBC ($8.80 \text{ m}^2 \text{ g}^{-1}$), which was directly prepared by carbonizing WS. This decrease in SSA may be attributed to the in situ Fe doping process (Kumar et al., 2020; Durga et al., 2024). As the temperature gradually increases, Fe_3O_4 magnetic particles are formed within the material and adhered to the biochar. Simultaneously, the introduction of internal magnetic particles increases the total micropore volume (V_{mic}) of MWSBC ($0.0020 \text{ cm}^3 \text{ g}^{-1}$) compared with that of WSBC ($0.0015 \text{ cm}^3 \text{ g}^{-1}$). Moreover, following the chitosan loading, the SSA further decreases to $0.91 \text{ m}^2 \text{ g}^{-1}$ (Xiao et al., 2019), indicating the strong crosslinking of chitosan with glutaraldehyde and its tight bonding with the MWSBC backbone (Kumar et al., 2024a). Along with the decrease in SSA, the lower pore volume confirms that the composites possess a compact crosslinked spatial structure, which is consistent with the SEM observations.

The crystal structure of the material at different stages was analyzed via X-ray diffraction (XRD). The results are shown in Fig. 2a. The

presence of peaks at 17° and 23° indicates that lignocellulose is the main constituent of WS (Morcillo-Martín et al., 2022). Upon carbonization, the diffraction peaks of WSBC become broader and lower, suggesting a reduction in the cellulose crystallinity and transformation into amorphous carbon. In the XRD pattern of MWSBC, characteristic peaks corresponding to the (220), (311), (400), (511), and (440) facets of Fe_3O_4 are observed at 30.31° , 35.64° , 43.38° , 57.51° , and 62.99° , respectively (Liu et al., 2023), which supports the successful synthesis of magnetic carbon (MWSBC) via carbonization. However, the intensity of the Fe_3O_4 peak in MWSBC-0.5 decreased after the loading of chitosan.

The surface functional groups and chemical bonds of WSBC, MWSBC, and MWSBC-0.5 were characterized using Fourier transform infrared spectroscopy (FT-IR). As shown in Fig. 2b, a wide absorption peak corresponding to the stretching vibration of O-H bonds appeared at 3424 cm^{-1} , and absorption peaks attributable to the stretching vibration of C-H bonds (Yang et al., 2020), were observed at 2969 cm^{-1} and 2877 cm^{-1} . An absorption peak located at $1624\text{--}1627 \text{ cm}^{-1}$ corresponds to the stretching of C=O bonds in the aromatic ring, and that at $1043\text{--}1058 \text{ cm}^{-1}$ is due to the stretching vibration of the C-O bond (Wang et al., 2022; Su et al., 2021). In the spectra of WSBC and MWSBC, the

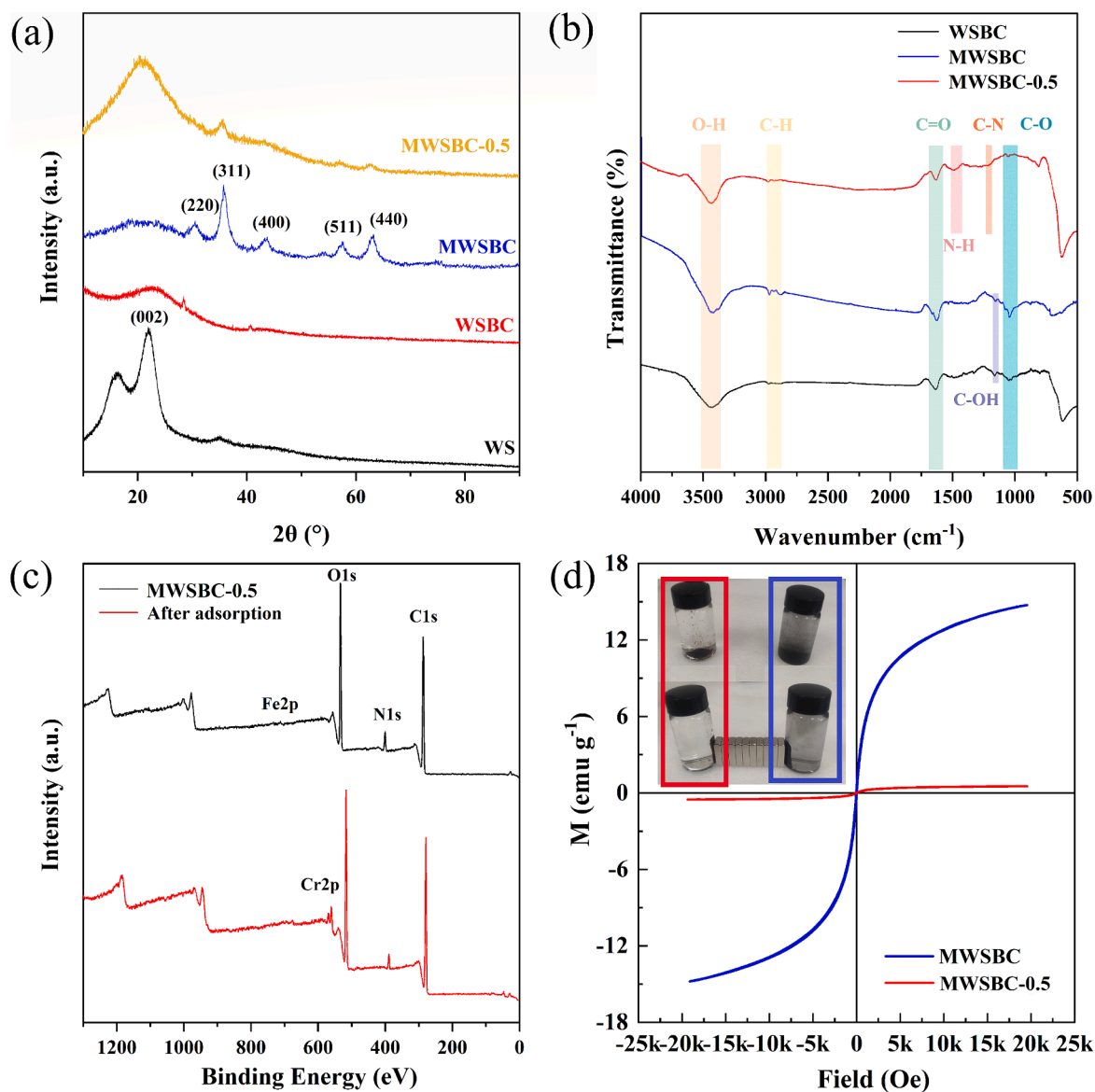


Fig. 2. (a) XRD patterns of WS, WSBC, MWSBC and MWSBC-0.5, (b) FT-IR spectra of WSBC, MWSBC and MWSBC-0.5, (c) XPS spectra of MWSBC-0.5 and after adsorption, (d) VSM curves of MWSBC and MWSBC-0.5.

stretching vibrations of the C–OH bonds produced absorption peaks in the range of 1159–1161 cm^{-1} . Upon magnetic loading, an absorption peak due to the stretching vibrations of the Fe–O groups appeared at 618 cm^{-1} (Azari et al., 2017). For MWSBC-0.5, absorption peaks ascribable to the stretching vibration of the N–H bond within the –NH amide bond II were observed around 1487 and 1521 cm^{-1} . Finally, a weak absorption peak at 1217 cm^{-1} confirmed the presence of a C–N (amino) bond, suggesting the successful glutaraldehyde crosslinking (Wu et al., 2022).

X-ray photoelectron spectroscopy (XPS) of the samples was performed to elucidate the surface chemical and electronic states of the composites before and after the adsorption of Cr(VI), and the results are presented in Fig. 2c. The XPS spectra revealed that the MWSBC-0.5 surface primarily comprised C, N, and O elements, which aligned well with the elemental analysis results. In addition, the Cr signal increased after adsorption, confirming that Cr was successfully adsorbed on the sample surface (Sun et al., 2023). According to the elemental analysis and XPS data (Table S3 and Table S4, Supporting Information), the content of chitosan, biochar, and Fe_3O_4 in the composite was estimated to be 77.22 %, 19.45 %, and 3.33 %, respectively. The high chitosan content substantially increases the number of available adsorption sites during the adsorption process. The magnetic properties of the samples were evaluated (Fig. 2d), finding that the saturation magnetization intensity of MWSBC was 14.78 emu g^{-1} , whereas that of MWSBC-0.5 decreased to 0.57 emu g^{-1} because of the inclusion of chitosan. This corresponded to the smaller characteristic peak of Fe observed in the XRD patterns. Although the reduction in magnetic properties slightly extended the duration of the magnetic recovery, they were still adequate for recovery.

3.2. Batch adsorption experiments

3.2.1. Comparison of Cr(VI) adsorption performance between different adsorbents

The adsorption capacity of the samples during each stage of the preparation process was examined, and the findings are illustrated in Fig. 3a. The adsorption capacity of WSBC for Cr(VI) without chitosan and magnetic particles was merely 6.3 mg g^{-1} . In contrast, the introduction of magnetic particles increased the adsorption capacity of MWSBC to 10.2 mg g^{-1} . The Cr(VI) adsorption capacities of the chitosan/biochar composite WSBC-0.5 and the chitosan/ Fe_3O_4 composite Fe_3O_4 -0.5 were determined to be 107.6 and 101.2 mg g^{-1} , respectively, revealing no remarkable improvement compared with that of pure chitosan. This lack of improvement can be attributed to the depletion of certain functional groups upon crosslinking and to the agglomerated nature of Fe_3O_4 , which are detrimental to the adsorption capacity. However, the composite strategy involving chitosan/biochar/ Fe_3O_4 effectively mitigated the loss caused by crosslinking and maximized the utilization of the biochar and Fe_3O_4 magnetic particles, considerably enhancing the adsorption capacity to 121.8 mg g^{-1} . Furthermore, the combination of chitosan and magnetic biochar increased the number of active sites and the variety of functional groups, facilitating the adsorption process. The synergistic effect of the composite containing chitosan, biochar, and Fe_3O_4 arose from the integration of the properties of the diverse components, resulting in superior adsorption capacity compared with the individual components (Qiu et al., 2024).

3.2.2. Effect of different adsorbent dosages

The Cr(VI) adsorption capacity of MWSBC-0.5 at different dosages is shown in Fig. 3b. The Cr(VI) removal efficiency of MWSBC-0.5 increased gradually from 12.7 % to 78 % as the adsorbent dosage was gradually

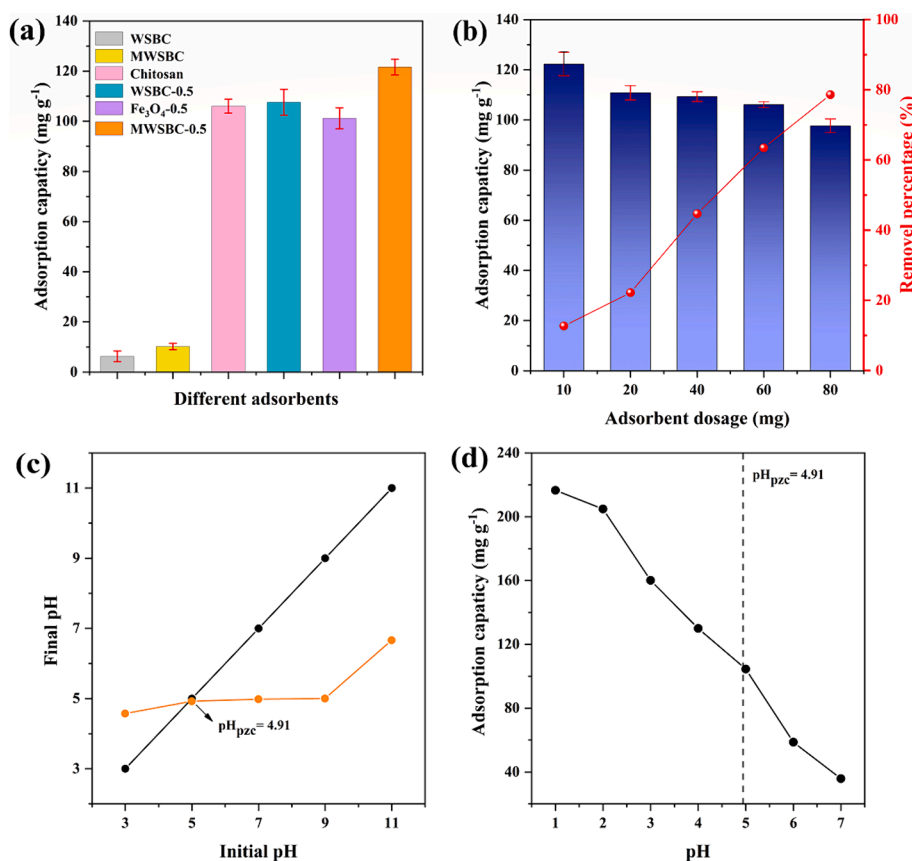


Fig. 3. (a) Adsorption capacities of WSBC, MWSBC, chitosan and MWSBC-0.5, (b) different adsorbent dosages of MWSBC-0.5, (c) the pH_{pzc} of MWSBC-0.5, (d) effect of pH on the adsorption capacities of MWSBC-0.5.

increased from 10 to 80 mg. Nonetheless, the adsorption capacity gradually decreased from 121.8 to 97.7 mg g⁻¹. Previous studies indicated that the removal efficiency increases with the adsorbent dosage and number of available adsorption sites, whereas the reduction in adsorption capacity is primarily attributed to the aggregation and overlap of adsorption sites (Wang et al., 2020).

3.2.3. Effect of pH

The pH value significantly influences the charge on the adsorbent surface, ionization degree, and morphological aspects of metal ions. Fig. 3d illustrates the adsorption capacity of MWSBC-0.5 for Cr(VI) at various pH values (1–7). The adsorption capacity was the highest at pH 1 (216.6 mg g⁻¹) and then gradually decreased with increasing pH until reaching a value of 35.9 mg g⁻¹ at pH 7. Normally, Cr(VI) exists in different forms depending on the pH value. Specifically, it exists mainly

as HCrO₄⁻ and Cr₂O₇²⁻ at pH < 6.5 and as CrO₄²⁻ and Cr₂O₇²⁻ at pH > 6.5. The adsorption free energy for HCrO₄⁻ is lower than that for Cr₂O₇²⁻ and CrO₄²⁻, indicating an easier removal for HCrO₄⁻ (Liu et al., 2023; Luo et al., 2022). In addition, the point of zero charge (pH_{PZC}) value of MWSBC-0.5 is 4.91. When the pH value was smaller than the pH_{PZC} value, the charge of the adsorbent surface was positive due to protonation, resulting in the electrostatic attraction of HCrO₄⁻ and Cr₂O₇²⁻, further increasing the adsorption performance. When the pH value was larger than pH_{PZC} value, the adsorbent surface was negatively charged, causing electrostatic repulsion that could decrease the adsorption capacity. For practical reasons, the pH value used in the subsequent adsorption experiment was that measured at the time of configuration (pH 5) and was not further adjusted.

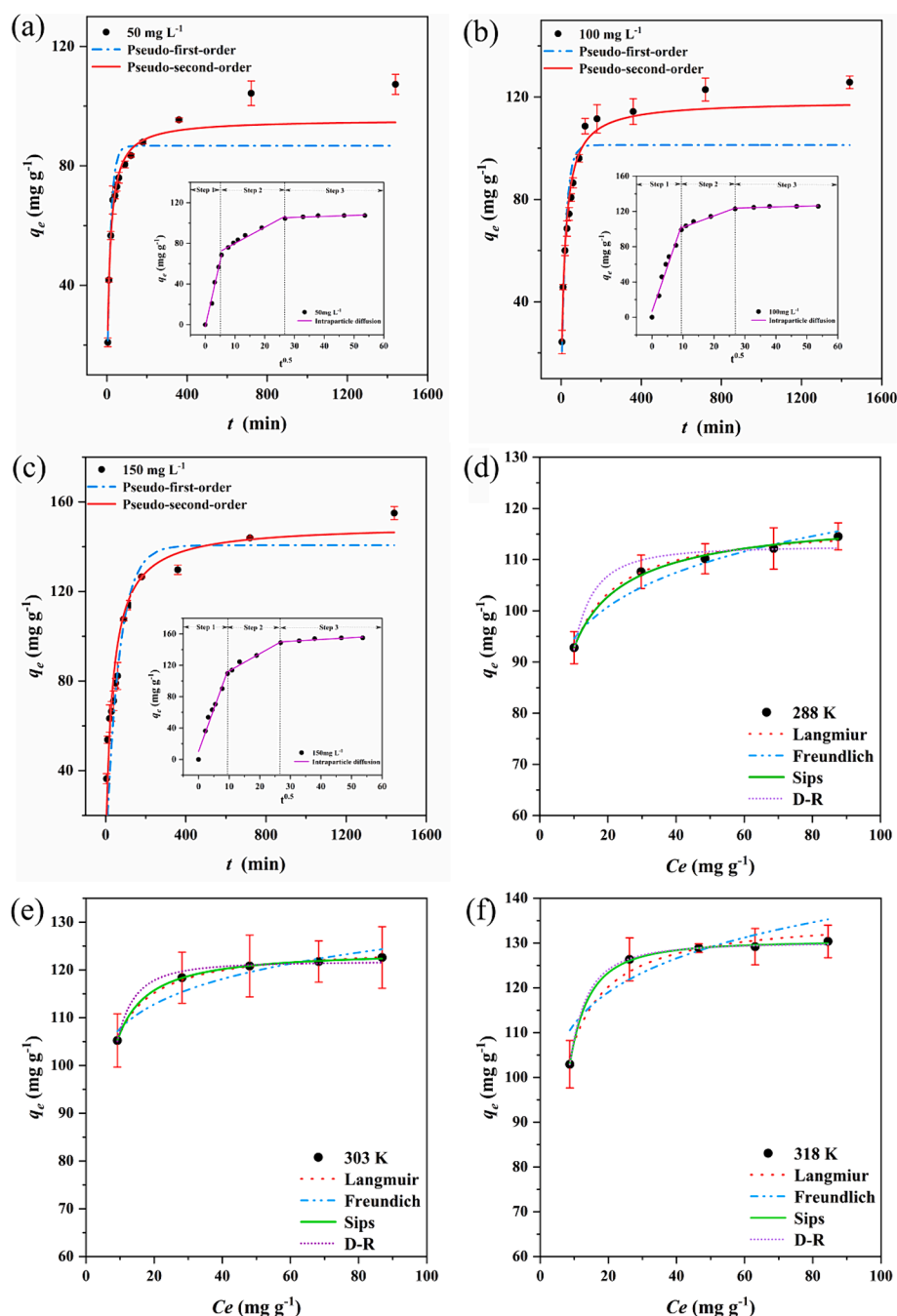


Fig. 4. The adsorption kinetics of MWSBC-0.5 at (a) 50 mg/L (b) 100 mg/L and (c) 150 mg/L. Adsorption isotherms at (d) 288 K (e) 303 K and (f) 318 K.

3.2.4. Adsorption kinetics

The adsorption kinetics of MWSBC-0.5 for Cr(VI) were examined at various concentrations (50, 100, 150 mg/L) to determine the relationship between the adsorption capacity and the duration of contact between the adsorbent and different initial concentrations. The results are presented in Fig. 4a, 4b, and 4c. Similar trends were observed for the Cr(VI) adsorption capacity of MWSBC-0.5 at different concentrations. At 50 mg/L, the adsorption capacity experienced a rapid increase within the first 60 min, followed by a gradual increase until reaching a plateau. At 100 and 150 mg/L, the rapid adsorption stage persisted for 120 min. Eventually, the adsorption equilibrium was achieved at approximately 1200 min.

The adsorption behavior of Cr(VI) on MWSBC-0.5 was evaluated on the basis of the nonlinear fitting of experimental data using several kinetic models. The obtained kinetic model parameters are shown in Table 1. The pseudo-first-order kinetic model exhibited higher correlation coefficient (R^2) values ranging from 0.959 to 0.984 than the pseudo-second-order kinetic model for all concentrations, and the calculated equilibrium adsorption capacity ($Q_{e,cat}$) value was closer to the experimental value. This indicated that the Cr(VI) adsorption on MWSBC-0.5 was a chemical adsorption process in which electrons were transferred and shared (Zhang et al., 2022b). To further analyze the adsorption process, an intraparticle diffusion model was employed. We successfully obtained at least two fitted lines, each with an R^2 value of 0.94 or higher. This demonstrates that the adsorption process comprised multiple stages. The first stage is a rapid adsorption stage, where a large number of available sites on the surface come into transient contact with Cr(VI), thus immobilizing Cr(VI) ions. The second stage is the main rate-limiting stage of the adsorption process, i.e., a gradual adsorption stage. At this stage, the Cr(VI) ions gradually diffuse from the outer surface of the adsorbent toward the inner contact. The final stage is the adsorption saturation stage. The adsorption of Cr(VI) on the adsorbent reaches saturation, and a dynamic equilibrium is attained between the adsorbent and the pollutant. However, the fitted line does not extend through the origin; therefore, intraparticle diffusion may not be the only rate-limiting step and other effects, such as membrane diffusion, may affect the adsorption process (Chen et al., 2021).

Table 1
Adsorption kinetic parameters of MWSBC-0.5.

Sample	Kinetic models	Parameter	Cr (VI) concentration C_0 (mg L ⁻¹)		
			50	100	150
		Q_e (mg g ⁻¹)	107.27	125.76	154.96
MWSBC-0.5	Pseudo-first-order	k_1 (min ⁻¹)	0.057	0.092	0.015
		$Q_{e,cat}$ (mg g ⁻¹)	86.69	101.22	140.60
		R^2	0.922	0.835	0.870
	Pseudo-second-order	k_2 (g mg ⁻¹ min ⁻¹)	0.0007	0.0003	0.0004
		$Q_{e,cat}$ (mg g ⁻¹)	95.47	118.35	149.77
		R^2	0.984	0.963	0.959
	Intraparticle diffusion	K_{p1} (mg g ⁻¹ min ^{-0.5})	12.91	10.24	10.83
		C_1	2.07	6.49	10.08
		R^2	0.978	0.956	0.962
		K_{p2} (mg g ⁻¹ min ^{-0.5})	1.59	1.30	2.19
		C_2	64.02	89.02	90.94
		R^2	0.948	0.958	0.968
		k_{p3} (mg g ⁻¹ min ^{-0.5})	0.0015	0.002	0.226
		C_3	107.22	125.68	143.85
		R^2	0.608	0.608	0.776

Experimental parameters: Temperature 303 K and experiment repeated three times.

3.2.5. Adsorption isotherm

The adsorption isotherms were examined to investigate the changes in the adsorption capacity and equilibrium concentration throughout the adsorption process (Fig. 4d, 4e, and 4f). The adsorption isotherms at 288, 303, and 318 K were analyzed and fitted using Langmuir, Freundlich, Sips, and Dubinin-Radushkevich models. The corresponding parameters are shown in Table 2. The adsorption gradually reached equilibrium with increasing concentration of Cr(VI) at different temperatures. The isotherm model fitting data suggested that the Langmuir isotherm exhibited R^2 values ranging from 0.96 to 0.99, indicating a monolayer adsorption. Using the obtained data, the R_L values, which represent unfavorable adsorption ($R_L > 1$), linear adsorption ($R_L = 1$), and favorable adsorption ($R_L < 1$), were calculated. The R_L values of MWSBC-0.5 fell within the range of 0–1, suggesting its favorable adsorption nature. To further understand the monolayer adsorption process, the Sips model was utilized, which is a three-parameter model suitable for monolayer adsorption. It proved that the adsorption process could be monolayer adsorption. In addition, the presence of an adsorbed molecule at the $1/n_s$ adsorption site of MWSBC-0.5 illustrates its surface heterogeneity (Wang and Guo, 2020). The n_s value corresponds to the curvature of the adsorption isotherm, which is related to the homogeneity and energy distribution of the adsorption process. The n_s values that vary with temperature in the fitted data are actually influenced by thermodynamics. Temperature can affect the interaction between adsorbent and adsorbate, which can alter the energy distribution of adsorption. An increase in temperature may increase the thermal movement of the adsorption sites, facilitating the penetration of Cr(VI) ions into these sites. The increase in the n_s value indicates that the adsorption process on the surface of MWSBC-0.5 is heterogeneous, which confirms the structural complexity of MWSBC-0.5.

3.2.6. Adsorption thermodynamics

The influence of temperature on the Cr(VI) adsorption efficiency of MWSBC-0.5 was examined by performing adsorption experiments at different temperatures (288, 303, and 318 K), and the results are depicted in Fig. 5a. As the temperature increased from 288 K to 318 K, the Cr(VI) adsorption capacity of MWSBC-0.5 increased from 114.52 to 130.36 mg g⁻¹. Thermodynamic equations were employed to analyze the parameters, and the results are presented in Table 3. The different temperatures yielded negative Gibbs free energy values of -0.47, -0.68, and -0.88 kJ mol⁻¹, respectively, implying that the adsorption was spontaneous. Meanwhile, a positive ΔH value of 3.503 kJ mol⁻¹ was obtained, indicating that the adsorption process was endothermic. The ΔS value (13.78 J mol⁻¹ K⁻¹) was positive, indicating that the interfacial randomness gradually increased (Qu et al., 2023).

3.2.7. Coexisting cations and ionic strength

Adsorbents used in practical applications are often influenced by background electrolytes and coexisting ions, which can affect the adsorption capacity of the adsorbent to different extents. In this study, several monovalent and divalent ions were selected to investigate their effects on the Cr(VI) adsorption capacity, and the results are shown in Fig. 5b. The effects on the adsorption capacity followed the order of $SO_4^{2-} > K^+ > Zn^{2+} > Mg^{2+} > NO_3^- > Cl^-$, demonstrating that higher valence anions such as SO_4^{2-} have a considerable impact on the Cr(VI) adsorption capacity of MWSBC-0.5. In general, higher valence cations interact more readily with the adsorbent surface because their covalent bonds and hydration are weaker. Consequently, the Cr(VI) adsorption capacity was reduced. Meanwhile, anions compete with cations (e.g., NH_4^+) on the adsorbent surface, decreasing the number of available interaction sites for Cr(VI) adsorption. Zhang et al. (2020) conducted an earlier study supporting these findings. The SO_4^{2-} ion substantially decreased the Cr(VI) adsorption capacity of MWSBC-0.5, while Cl^- and NO_3^- ions decreased it slightly. The SO_4^{2-} and $Cr_2O_7^{2-}$ ions have similar molecular structures and negative charges; thus, their competition was

Table 2
Adsorption isotherms parameters of MWSBC-0.5.

Sample	Isotherm types	Constants	288 K	303 K	318 K
			MWSBC-0.5	Langmuir	Q_m (mg g ⁻¹)
		K_L (L/mg)	0.38	0.58	0.36
		R_L	0.02–0.11	0.017–0.07	0.02–0.12
		R^2	0.991	0.998	0.960
	Freundlich	K_F (mg g ⁻¹ (L/mg) ^{1/n})	75.61	90.83	95.17
		n_F	10.49	14.67	9.67
		R^2	0.937	0.889	0.691
	Sips	Q_m (mg g ⁻¹)	123.09	129.63	144.31
		K_s (L ^{1/n} mg ⁻ⁿ)	0.198	0.234	0.048
		n_s	1.33	1.46	2.02
		R^2	0.990	0.995	0.998
	D-R	Q_m (mg g ⁻¹)	112.27	121.73	130.11
		ϵ	0.0008–0.0569	0.0008–0.0674	0.0008–0.0752
		K_{DR} (mol ² kJ ⁻²)	3.38	2.18	3.12
		R^2	0.938	0.98	0.997

Experimental parameters: The initial concentration of Cr(VI) was 100 mg/L and the experiment was repeated three times.

more obvious. Finally, cations such as K⁺ and Zn²⁺ may coordinate with anionic chromates such as CrO₄²⁻ and Cr₂O₇²⁻ according to the Lewis acid–base theory, which may further affect the Cr(VI) removal effect. Fig. 5c shows the effect of NaCl ionic strength on the Cr(VI) removal by MWSBC-0.5. As the ionic strength increased from 0.001 to 0.5 M, the Cr(VI) removal efficiency of MWSBC-0.5 decreased from 96.8 % to 47.8 %, which can be attributed to the competition and interaction between ions and the available adsorption sites.

3.2.8. Reusability experiments

Reusability is an important factor for evaluating the cost-effectiveness and environmental friendliness of an adsorbent. The results in Fig. 5d show that hydrochloric acid (HCl) is a good eluent for regeneration because it can protonate the functional groups of MWSBC-0.5 in addition to desorbing Cr. HCl can desorb Cr ions from composites by interacting with functional groups on the adsorbent, leading to dissociation or protonation of the functional groups by H⁺ (Dhal et al., 2018). After the first cycle, the Cr(VI) removal efficiency of MWSBC-0.5 was 94.8 %, which was higher than the initial removal (zero cycle) of 82.5 % (Fig. 5e). This indicates that the protonated functional groups successfully increased the adsorption performance. Additionally, the residual performance indicators of the adsorbents were compared. Taking the zero cycle as a reference point of 100 %, the removal rate and residual performance were maintained at 51.9 % and 78.6 %, respectively, after seven cycles (Fig. 5f). In contrast, a decreasing trend in the removal rate and residual performance of both WSBC-0.5 and Fe₃O₄-0.5 was observed in the sixth cycle, especially for Fe₃O₄-0.5. The HCl elution caused the leaching of some agglomerated Fe₃O₄ nanoparticles, which decreased the activity, removal rate, and residual performance. Moreover, the regeneration of chitosan-based modified materials considerably decreases with increasing number of reusability cycles, which can be attributed to the loss of adsorption sites and the hydrolysis of polysaccharides (da Silva Alves et al., 2021). However, the decrease in both the removal rate and residual performance of MWSBC-0.5 was minimal. This result demonstrates the success of the composite strategy, which can be mainly attributed to the following reasons:

1. The presence of Fe₃O₄ attached on biochar effectively prevents the agglomeration phenomenon and significantly reduces the loss of Fe during elution
2. Although the regeneration of the adsorbent causes the hydrolysis of chitosan and a reduction in the number of adsorption sites, the tightly crosslinked network of MWSBC-0.5 exposes new adsorption sites layer by layer, compensating the loss in adsorption capacity.
3. The combination of chitosan and magnetic biochar exhibits a beneficial synergistic effect. The introduction of magnetic biochar

facilitates the recovery of the composite material by applying an external magnetic field. Chitosan effectively encapsulates the magnetic biochar, preventing the detachment of magnetic nanoparticles from the carrier during adsorption and subsequent reuse. Furthermore, chitosan, biochar, and magnetic nanoparticles are effective in adsorbing heavy metal ions. As a result of this design, the prepared composite material exhibits high adsorption capacity and good recyclability.

The adsorption capacity of MWSBC-0.5 is notably influenced by its positively charged surface (Zang et al., 2024). Treatment with HCl solution remarkably reduced the pH_{pZC} value of MWSBC-0.5 from 4.91 to 2.27, indicating an increased protonation of the amino and hydroxyl groups on the surface, which becomes more positively charged. This substantially boosts the electrostatic attraction. Furthermore, MWSBC-0.5 can lower the pH value of the adsorption environment. The adjustment of pH is crucial as it converts more of the Cr ions in solution to HCrO₄⁻, thus enhancing the electrostatic attraction on MWSBC-0.5. In the later cycles, the exposed surfaces of the crosslinked chitosan and magnetic biochar were protonated because of the gradual hydrolysis of chitosan. The synergistic effect of altering the surface charge and regulating the pH value of the environment is essential for improving the reusability of MWSBC-0.5. This dual-action approach not only enhances its performance but also ensures its consistency and effectiveness during repeated cycles of use. Thus, the tightly crosslinked composite structure plays a key role in the regeneration of the adsorbent. In summary, to ensure an optimal performance, the adsorbent should be regenerated less than seven times.

3.2.9. Removal of low concentrations of Cr(VI)

To accurately mimic the elimination of Cr(VI) in a natural setting, the capability of MWSBC-0.5 to remove low concentrations of Cr(VI) was investigated by simulating lake water conditions. The results are presented in Fig. 5g. Without any external factors, MWSBC-0.5 reduced the concentration of Cr(VI) in deionized water to below the World Health Organization discharge standards after 113 min. However, it took 235 min to achieve the same outcome using the simulated lake water. Therefore, in practice, depending on the complexity of the water matrix, the removal of Cr(VI) by the composites may require more than 113 min. In complex water matrices, the primary factors affecting the Cr(VI) removal rate were the extent of contact between the adsorption sites and contaminants, the pH of the solution, and the presence of coexisting ions (Wan et al., 2023). Consequently, the removal time increased by 2.07 times. However, the ability of MWSBC-0.5 to treat contaminated complex water matrices is noteworthy.

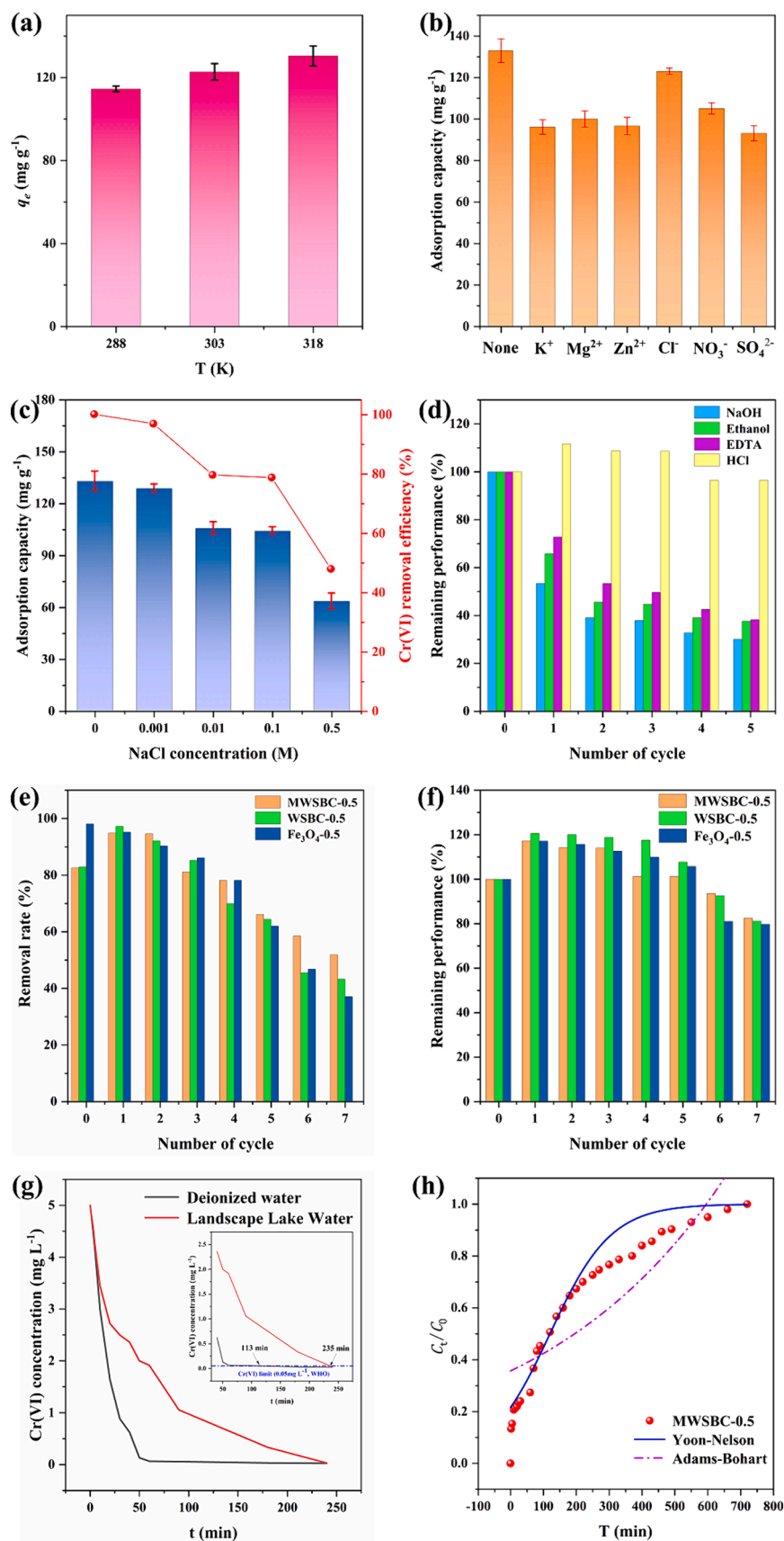


Fig. 5. (a) Effect of temperature, (b) effect of coexisting cations, (c) effect of NaCl ionic strength, (d) effect of different eluents on the reusability of MWSBC-0.5, (e) and (f) reusability of MWSBC-0.5, (g) removal of low concentration of Cr(VI) by MWSBC-0.5 in different water bodies, (h) Fixed-bed experiment of MWSBC-0.5.

Table 3
Adsorption Thermodynamics parameters of MWSBC-0.5.

Adsorbent	T (K)	ΔG (kJ/mol)	ΔH (kJ/mol)	ΔS (J mol ⁻¹ K ⁻¹)
MWSBC-0.5	288	-0.47	3.50	13.78
	303	-0.68		
	318	-0.88		

Experimental parameters: The initial concentration of Cr(VI) was 100 mg/L and the experiment was repeated three times.

3.2.10. Fixed-bed column experiment

We conducted a brief simulation of fixed-bed column experiments to investigate the potential of MWSBC-0.5 for industrial applications. The breakthrough curve of MWSBC-0.5 for Cr(VI) is depicted in Fig. 5h. The assessment of the adsorption process penetration and saturation was based on the time it took for the ratio of C_t/C_0 to reach 0.2 and 0.8. As the duration of the adsorption experiment increased to 370 min, the ratio of C_t/C_0 reached 0.8. However, the adsorption process did not reach completion until approximately 720 min. This suggests that MWSBC-0.5 possesses a considerable number of adsorption sites, which further prolonged the adsorption time. By fitting the Yoon–Nelson model (Table S5, Supporting Information), a relatively good R^2 value of 0.926 was obtained. This result implies that the adsorption characteristics of MWSBC-0.5 in the mobile phase can be elucidated by the diminished likelihood of adsorption for an individual adsorbent molecule (Cr), which is connected to both the breakthrough of the adsorbent (MWSBC-0.5) and its adsorption probability (Zoroufchi Benis et al., 2023).

3.2.11. Comparison with other chitosan-containing adsorbents

The structure of MWSBC-0.5 is critical for its excellent adsorption and reusability performance. Some recent studies on Cr(VI) adsorption and chitosan-based adsorbents are listed in Tables 4 and 5, respectively. The adsorption capacity of MWSBC-0.5 was considerably higher than those of previously reported adsorbents. In particular, MWSBC-0.5 exhibited better adsorption efficiency and performance during several cycles, outperforming other adsorbents in the same cycle. This comparison proves the effectiveness of the improved structure based on layer-by-layer exposure, which retains the rich chemical surface of chitosan for an efficient Cr(VI) removal. The layer-by-layer exposure also avoids the one-time loss of active sites, effectively enhancing the reusability. Furthermore, studies in this field generally focus on adsorption processes within a specific pH range, thus overlooking the variable pH values in real environments. Several studies have underscored the relevance of maintaining a low pH for an effective Cr(VI) removal. Notably, MWSBC-0.5 exhibited superior adsorption

Table 4
Comparison of adsorption capacity of MWSBC-0.5 with other adsorbents.

Adsorbent	Cr(VI) concentration (mg/L)	pH value	Q_{max} (mg g ⁻¹)	Reference
CSG@AAB	10	4.0	5.0	(El Kaim Billah et al., 2024)
MnFe ₂ O ₄ @Fh-EDA	–	5	51.36	(Shen et al., 2023)
Fe ₂ O ₃ /Fe ₃ O ₄ /WBC	100	–	55	(Bai et al., 2021)
CoFe ₂ O ₄ @UiO-66-NH ₂ -PDA/ β -CD-TEPA	–	2	96.2	(Liu and Hu, 2023)
PPy/DT	50	2.0	99.43	(Mazkad et al., 2024)
MAF-LDOs	100	3	122.85	(Mo et al., 2023)
MWSBC-0.5	100	1	216.6	This study
		5	121.8	

performance compared with other adsorbents at pH 5 and 1, demonstrating its overall superiority. Furthermore, the composites created using this construction of special structures are anticipated to provide more stable performance in drug delivery and energy storage in comparison to other materials, owing to their improved stability.

3.3. Possible adsorption mechanism

Surface functional groups play a crucial role in the adsorption process. Consequently, the Cr(VI) removal by MWSBC-0.5 induced changes in the surface functional groups, according to the FT-IR results (Fig. 6a). The O–H band near 3424 cm⁻¹ underwent a redshift after the adsorption of Cr(VI), suggesting that O–H strongly interacts with Cr(VI). Moreover, the attenuation of the C=O, N–H, and C–N peaks at 1624, 1479, and 1201 cm⁻¹, respectively, suggests the active participation of these groups in the adsorption procedure, while –NH₂, –OH, and other functional groups can form complexes with Cr(VI).

The adsorption mechanism was further explored by analyzing the high-resolution XPS spectra of MWSBC-0.5 before and after the adsorption of Cr(VI), as depicted in Fig. 6b, 6c, 6d, 6e, and 6f. The C1s spectrum of MWSBC-0.5 after adsorption exhibits a novel peak at 288.3 eV, which corresponds to a new complex, namely Cr(CO)₆ (Zhang et al., 2015). Notably, the C=O peak at 286.4 eV and the C–N peak at 287.9 eV are substantially diminished due to complexation and reduction, among other effects. In the N1s spectrum, peaks attributable to amino and protonated amino groups on the MWSBC-0.5 surface were observed at 399.6 and 402.1 eV, respectively. A remarkable reduction in the peak area corresponding to O–H at approximately 533.1 eV in the O1s spectrum strongly indicates that O–H groups serve as primary active sites for Cr(VI) adsorption. This observation aligns well with the FT-IR results. In addition, influenced by the pH value of the solution, the amino groups and O–H not only play a crucial role in the complexation and reduction processes but also undergo protonation. Owing to this protonation, the adsorbent surface becomes positively charged, which enhances the electrostatic attraction of the material. This could be an ancillary yet important mechanism in the adsorption dynamics. Another benefit of the nitrogen-containing moiety is the increased hydrophilicity of the MWSBC-0.5 surface, which increases the probability of contact between Cr(VI) ions and the internal pores and active sites of MWSBC-0.5 in the liquid-phase environment, thereby facilitating the Cr(VI) adsorption (Yuan et al., 2023).

After the Cr(VI) adsorption, two additional peaks, namely Cr2p_{3/2} and Cr2p_{1/2}, become prominent in the Cr2p spectrum of MWSBC-0.5. These peaks can be further deconvoluted into two peaks at 587.3 and 578.07 eV, corresponding to Cr(VI), and two peaks at 586.4 and 576.8 eV, corresponding to Cr(III) (Kuang et al., 2023). These findings align with earlier descriptions and provide evidence of the occurrence of a reduction process during the adsorption of Cr(VI) on MWSBC-0.5. Furthermore, the intensities of the O–H peak at 533.1 eV and the Fe–O peak at 533.8 eV in the O1s spectrum decrease because of reduction. The presence of certain functional groups such as C–O and Fe(II) ions on the MWSBC-0.5 surface facilitates this reduction process. After reduction, both Cr(III) and Cr(VI) cations are present in the solution. These cations may undergo cation exchange with Fe(II) and Fe(III), which are also present on MWSBC-0.5 (Wang et al., 2023d). The XPS analysis showed that the weakening of the Fe(II) ion signal on MWSBC-0.5 could be caused by both reduction and cation exchange processes, whereas the Cr(III) signal after adsorption could be caused by multiple reactive processes, including electrostatic attraction, cation exchange, and complexation.

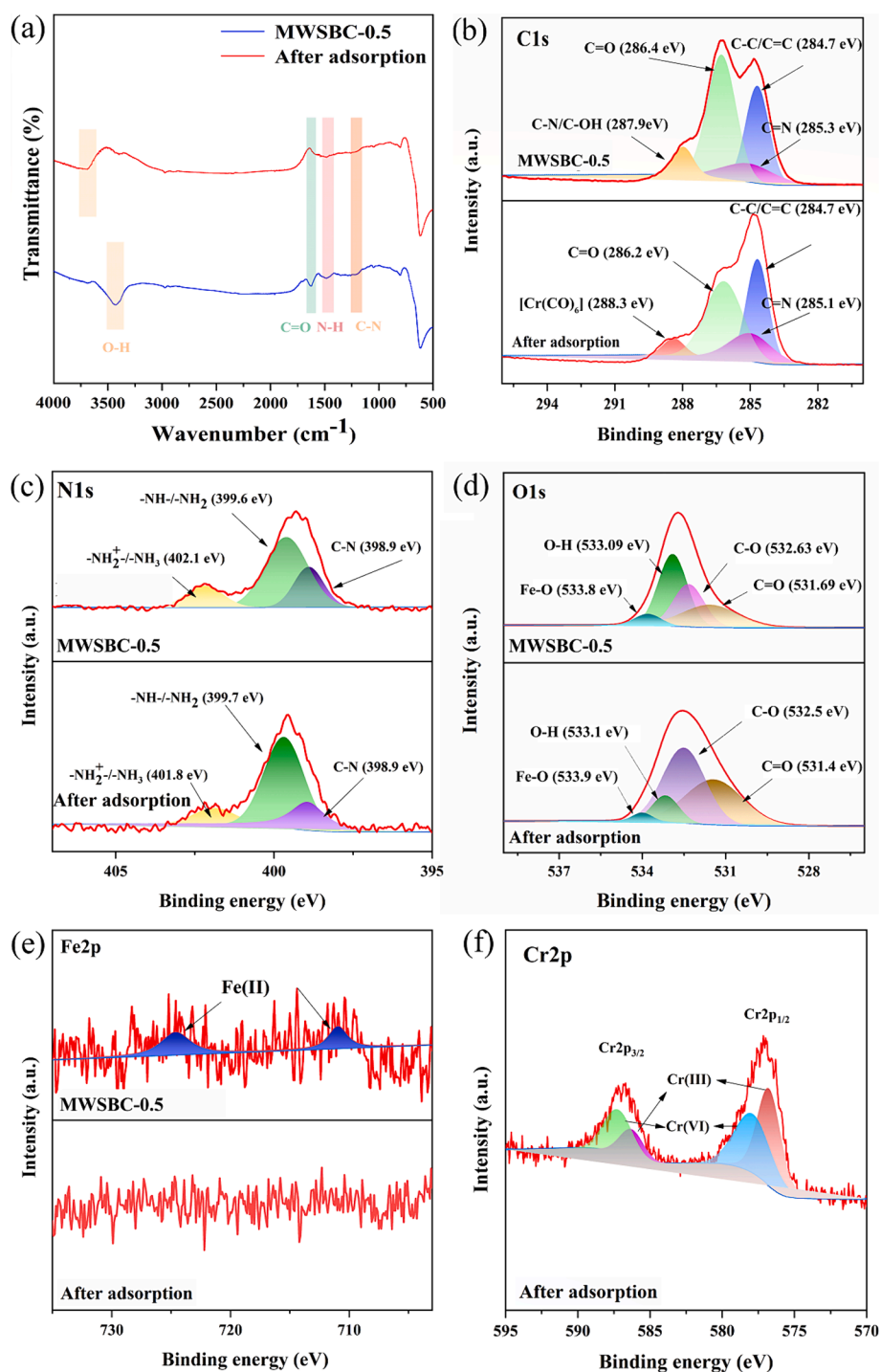
In general, the process of Cr(VI) removal on MWSBC-0.5 is not dictated by a singular mechanism; instead, it involves a combination of physical and chemical mechanisms (Fig. 7). The principal adsorption mechanisms can be categorized into four types: reduction, complexation, cation exchange, and electrostatic attraction.

Table 5

Comparison of maximum adsorption capacity and reusability efficiency of different chitosan-loaded materials for Cr(VI) removal.

Adsorbent	Cr(VI) concentration (mg/L)	pH value	Q_{max} (mg g ⁻¹)	Number of cycles	Remaining performance (%)	Reference
CMLB	40	3.0	30.14	3	72 %	(Xiao et al., 2019)
OCS-160	100	3.0	83.6	5	Less than 40 %	(Luo et al., 2022)
FSBC(1:1:1)	-	4.5	101.38	5	69.5 %	(Yang et al., 2021)
CMPBC	5	3.0	14.6	-	-	(Perera et al., 2023)
Ch-ASC400	55	1.5	37.48	-	-	(Altun et al., 2021)
MWSBC-0.5	50	5	80.79	7	78.6 %	This study

Experimental parameters: Temperature 303 K and experiment repeated three times.

**Fig. 6.** (a) FT-IR spectra of MWSBC-0.5 and after adsorption. XPS spectra of MWSBC-0.5 and after adsorption (b) C1s (c) N1s (d) O1s (e) Fe2p.

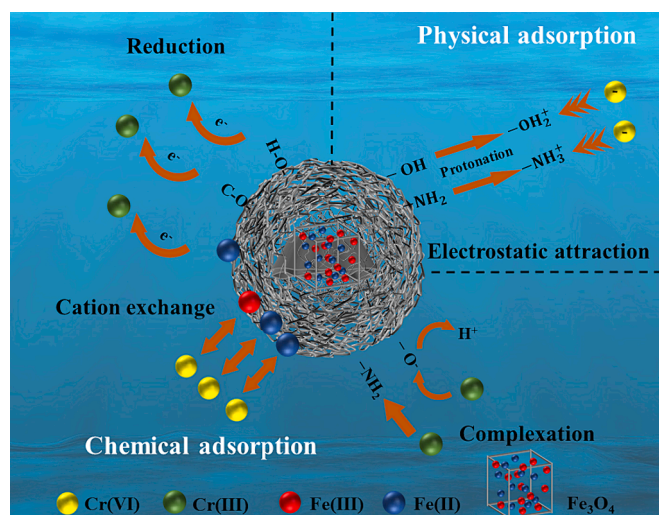


Fig. 7. Schematic of adsorption mechanism.

4. Conclusion

A MWSBC-0.5 composite consisting of chitosan and magnetic biochar was prepared, and a tightly interconnected structure was successfully constructed by adjusting the proportion of chitosan. Characterization confirmed that the material was rich in functional groups and adsorbed 121.8 mg g^{-1} of Cr(VI) in water, which was further enhanced to 216.6 mg g^{-1} at $\text{pH} = 1$. The pseudo-second-order kinetic and Sips isotherm models revealed the heterogeneous chemisorption behavior of MWSBC-0.5. The experiments on reusability confirmed a retention rate of 78.6 % after seven cycles. The performance in the fixed-bed column experiment and real water simulation was also satisfactory. Several potential adsorption mechanisms were proposed, including electrostatic attraction, cation exchange, complexation, and reduction. In conclusion, this study provides valuable insights into the design and preparation of high-performance adsorbents from agricultural waste such as WS to address sustainability challenges.

CRedit authorship contribution statement

Yongbo Yu: Conceptualization, Formal analysis, Investigation, Methodology, Writing – original draft. **Wanting Liu:** Formal analysis, Investigation. **Yinuo Zhang:** Formal analysis, Investigation. **Bolun Zhang:** Formal analysis. **Yiping Jin:** Visualization. **Siji Chen:** Validation. **Shanshan Tang:** Conceptualization, Data curation, Methodology, Project administration, Resources, Writing – review & editing. **Yingjie Su:** Resources. **Xiaoxiao Yu:** Formal analysis. **Guang Chen:** Supervision.

Declaration of competing interest

The authors declare that they have no known competing financial interests or personal relationships that could have appeared to influence the work reported in this paper.

Acknowledgments

This work was supported by a program grant (Project No. 20230202073NC) from the Jilin Province science and technology development plan.

Appendix A. Supplementary data

Supplementary data to this article can be found online at <https://doi.org/10.1016/j.arabjc.2024.105746>.

[org/10.1016/j.arabjc.2024.105746](https://doi.org/10.1016/j.arabjc.2024.105746).

References

- Altun, T., Ecevit, H., Kar, Y., Çiftçi, B., 2021. Adsorption of Cr(VI) onto cross-linked chitosan-almond shell biochars: equilibrium, kinetic, and thermodynamic studies. *J. Anal. Sci. Technol.* 12, 38. <https://doi.org/10.1186/s40543-021-00288-0>.
- An, T., Chang, Y., Xie, J., Cao, Q., Liu, Y., Chen, C., 2022. Deciphering physicochemical properties and enhanced microbial electron transfer capacity by magnetic biochar. *Bioresour. Technol.* 363, 127894 <https://doi.org/10.1016/j.biortech.2022.127894>.
- Anil Kumar, Y., Dasha Kumar, K., Kim, H.-J., 2020. Facile preparation of a highly efficient NiZn₂O₄-NiO nanoflower composite grown on Ni foam as an advanced battery-type electrode material for high-performance electrochemical supercapacitors. *Dalton Trans.* 49, 3622–3629. <https://doi.org/10.1039/D0DT00268B>.
- Anil Kumar, Y., Kim, H.J., 2018a. Effect of time on a hierarchical corn skeleton-like composite of CoO@ZnO as capacitive electrode material for high specific performance supercapacitors. *Energies (Basel)* 11, 3285. <https://doi.org/10.3390/en11123285>.
- Anil Kumar, Y., Kim, H.-J., 2018b. Preparation and electrochemical performance of NiCo₂O₄@NiCo₂O₄ composite nanoplates for high performance supercapacitor applications. *New J. Chem.* 42, 19971–19978. <https://doi.org/10.1039/C8NJ05401K>.
- Azari, A., Gharibi, H., Kakavandi, B., Ghanizadeh, G., Javid, A., Mahvi, A.H., Sharafi, K., Khosravi, T., 2017. Magnetic adsorption separation process: an alternative method of mercury extracting from aqueous solution using modified chitosan coated Fe₃O₄ nanocomposites. *J. Chem. Technol. Bio.* 92, 188–200. <https://doi.org/10.1002/jctb.4990>.
- Bai, L., Su, X., Feng, J., Ma, S., 2021. Preparation of sugarcane bagasse biochar/nano-iron oxide composite and mechanism of its Cr(VI) adsorption in water. *J. Clean Prod.* 320, 128723 <https://doi.org/10.1016/j.jclepro.2021.128723>.
- Cao, W., Animasau, I.L., Yook, S.J., Oladipupo, V.A., Ji, X., 2022. Simulation of the dynamics of colloidal mixture of water with various nanoparticles at different levels of partial slip: Ternary-hybrid nanofluid. *Int. Commun. Heat. Mass.* 135, 106069 <https://doi.org/10.1016/j.icheatmasstransfer.2022.106069>.
- Chen, B., Zhao, H., Chen, S., Long, F., Huang, B., Yang, B., Pan, X., 2019. A magnetically recyclable chitosan composite adsorbent functionalized with EDTA for simultaneous capture of anionic dye and heavy metals in complex wastewater. *Chem. Eng. J.* 356, 69–80. <https://doi.org/10.1016/j.cej.2018.08.222>.
- Chen, L., Zhu, Y., Cui, Y., Dai, R., Shan, Z., Chen, H., 2021. Fabrication of starch-based high-performance adsorptive hydrogels using a novel effective pretreatment and adsorption for cationic methylene blue dye: Behavior and mechanism. *Chem. Eng. J.* 405, 126953 <https://doi.org/10.1016/j.cej.2020.126953>.
- Chin, J.F., Heng, Z.W., Teoh, H.C., Chong, W.C., Pang, Y.L., 2022. Recent development of magnetic biochar crosslinked chitosan on heavy metal removal from wastewater – Modification, application and mechanism. *Chemosphere* 291, 133035. <https://doi.org/10.1016/J.CHEMOSPHERE.2021.133035>.
- da Silva Alves, D.C., Healy, B., Pinto, L.A. de A., Cadaval, T.R.S., Breslin, C.B., 2021. Recent developments in Chitosan-based adsorbents for the removal of pollutants from aqueous environments. *Molecules* 26, 594. <https://doi.org/10.3390/molecules26030594>.
- Dhal, B., Abhilash, Pandey, B.D., 2018. Mechanism elucidation and adsorbent characterization for removal of Cr(VI) by native fungal adsorbent. *Sustainable Environ. Res.* 28, 289–297. <https://doi.org/10.1016/j.serj.2018.05.002>.
- Durga, I.K., Kulurumotlakatla, D.K., Ramachandran, T., Kumar, Y.A., Reddy, D.A., Raghavendra, K.V.G., Alothman, A.A., Rao, S.S., 2024. Synergy unleashed: NiMoO₄/WO₃/NF nanoflowers elevate for supercapacitor performance. *J. Phys. Chem. Solid* 186, 111811. <https://doi.org/10.1016/j.jpics.2023.111811>.
- El Kaim Billah, R., Islam, M.A., Nazal, M.K., Bahsis, L., Soufiane, A., Abdellaoui, Y., Achak, M., 2024. A novel glutaraldehyde cross-linked chitosan/acid-activated bentonite composite for effective Pb(II) and Cr(VI) adsorption: Experimental and theoretical studies. *Sep. Purif. Technol.* 334, 126094 <https://doi.org/10.1016/j.seppur.2023.126094>.
- Gao, N., Du, W., Zhang, M., Ling, G., Zhang, P., 2022. Chitosan-modified biochar: Preparation, modifications, mechanisms and applications. *Int. J. Biol. Macromol.* 209, 31–49. <https://doi.org/10.1016/j.ijbiomac.2022.04.006>.
- Grimshaw, P., Calo, J.M., Hradil, G., 2011. Cyclic electrowinning/precipitation (CEP) system for the removal of heavy metal mixtures from aqueous solutions. *Chem. Eng. J.* 175, 103–109. <https://doi.org/10.1016/j.cej.2011.09.062>.
- Hegazy, H.H., Sana, S.S., Ramachandran, T., Kumar, Y.A., Kulurumotlakatla, D.K., Abd-Rabboh, H.S.M., Kim, S.C., 2023. Covalent organic frameworks in supercapacitors: Unraveling the pros and cons for energy storage. *J. Energy Storage* 74, 109405. <https://doi.org/10.1016/j.est.2023.109405>.
- Huang, H., Guo, T., Wang, K., Li, Y., Zhang, G., 2021. Efficient activation of persulfate by a magnetic recyclable rape straw biochar catalyst for the degradation of tetracycline hydrochloride in water. *Sci. Total Environ.* 758, 143957 <https://doi.org/10.1016/j.scitotenv.2020.143957>.
- Islam, M.M., Mohana, A.A., Rahman, M.A., Rahman, M., Naidu, R., Rahman, M.M., 2023. A comprehensive review of the current progress of chromium removal methods from aqueous solution. *Toxics* 11, 252. <https://doi.org/10.3390/toxics11030252>.
- Kuang, Q., Liu, K., Wang, Q., Chang, Q., 2023. Three-dimensional hierarchical pore biochar prepared from soybean protein and its excellent Cr(VI) adsorption. *Sep. Purif. Technol.* 304, 122295 <https://doi.org/10.1016/j.seppur.2022.122295>.

- Kumar, Y.A., Kumar, K.D., Kim, H.-J., 2020. Reagents assisted ZnCo₂O₄ nanomaterial for supercapacitor application. *Electrochim. Acta* 330, 135261. <https://doi.org/10.1016/j.electacta.2019.135261>.
- Kumar, Y.A., Kullurumotlakatla, D.K., Park, I.-K., 2023b. Interface engineering for enhancing the performance of novel sodium-doped MoS₂ nanocomposite: Synthesis and characterization functioning as a high-performance supercapacitor. *Korean J. Chem. Eng.* 40, 2847–2854. <https://doi.org/10.1007/s11814-023-1556-2>.
- Kumar, K.D., Kumar, Y.A., Ramachandran, T., Al-Kahtani, A.A., Kang, M.C., 2023a. Cactus-Like Ni-Co/Co/Mn₂O₄ composites on Ni foam: Unveiling the potential for advanced electrochemical materials for pseudocapacitors. *Mater. Sci. Eng. B* 296, 116715. <https://doi.org/10.1016/j.mseb.2023.116715>.
- Kumar, K.D., Ramachandran, T., Kumar, Y.A., Mohammed, A.A.A., Kang, M., 2024a. Hierarchically fabricated nano flakes-rod-like CoMoO-S supported Ni-foam for high-performance supercapacitor electrode material. *J. Phys. Chem. Solid* 185, 111735. <https://doi.org/10.1016/j.jpccs.2023.111735>.
- Kumar, Y.A., Reddy, G.R., Ramachandran, T., Kullurumotlakatla, D.K., Abd-Rabboh, H.S. M., Abdel Hafez, A.A., Rao, S.S., Joo, S.W., 2024b. Supercharging the future: MOF-2D MXenes supercapacitors for sustainable energy storage. *J. Energy Storage* 80, 110303. <https://doi.org/10.1016/j.est.2023.110303>.
- Langård, S., Costa, M., 2015. Chromium, in: *Handbook on the Toxicology of Metals: Fourth Edition*. Elsevier Inc., pp. 717–742. <https://doi.org/10.1016/B978-0-444-59453-2.00033-0>.
- Lee, S., Hao, L.T., Park, J., Oh, D.X., Hwang, D.S., 2023. Nanochitin and Nanochitosan: Chitin Nanostructure Engineering with Multiscale Properties for Biomedical and Environmental Applications. *Adv. Mater.* 35, 2203325. <https://doi.org/10.1002/adma.202203325>.
- Liu, F., Hu, B., 2023. Experimental and DFT study of adsorption-reduction mechanism of Au(III) and Cr(VI) by β -cyclodextrin/polydopamine coated UiO-66-NH₂ magnetic composites. *Appl. Surf. Sci.* 626, 157292. <https://doi.org/10.1016/j.apsusc.2023.157292>.
- Liu, L., Sun, P., Chen, Y., Li, X., Zheng, X., 2023. Distinct chromium removal mechanisms by iron-modified biochar under varying pH: Role of iron and chromium speciation. *Chemosphere* 331, 138796. <https://doi.org/10.1016/j.chemosphere.2023.138796>.
- Luo, L., Cheng, S., Yue, L., You, Z., Cai, J., 2022. N-doped biochar from chitosan gel-like solution: effect of hydrothermal temperature and superior aqueous Cr(VI) removal performance. *Colloids Surf. A Physicochem. Eng. Asp.* 641, 128426. <https://doi.org/10.1016/j.colsurfa.2022.128426>.
- Ma, H., Wang, Q., Hao, Y., Zhu, C., Chen, X., Wang, C., Yang, Y., 2020. Fenton reaction induced in-situ redox and re-complexation of polyphenol-Cr complex and their products. *Chemosphere* 250, 126214. <https://doi.org/10.1016/j.chemosphere.2020.126214>.
- Mazkaf, D., El Idrissi, A., Marrane, S.E., Lazar, N., El Ouardi, M., Dardari, O., Channab, B.-E., Layaichi, O.A., Farsad, S., Baqais, A., Lotfi, E.M., Ahsaine, H.A., 2024. An innovative diatomite-polypyrrole composite for highly efficient Cr(VI) removal through optimized adsorption via surface response methodology. *Colloids Surf. A Physicochem. Eng. Asp.* 133172. <https://doi.org/10.1016/j.colsurfa.2024.133172>.
- Mo, H., Qiu, J., Yang, C., Zang, L., Sakai, E., 2020. Preparation and characterization of magnetic porous biochar for cellulose immobilization by physical adsorption. *Cellul.* 27, 4963–4973. <https://doi.org/10.1007/s10570-020-03125-6>.
- Mo, W., Yang, Y., He, C., Huang, Y., Feng, J., 2023. Excellent adsorption properties of Mg/Al/Fe LDs for Cr(VI) in water. *J. Environ. Chem. Eng.* 11, 111069. <https://doi.org/10.1016/j.jece.2023.111069>.
- Morillo-Martin, R., Espinosa, E., Rabasco-Vilchez, L., Sanchez, L.M., de Haro, J., Rodríguez, A., 2022. Cellulose nanofiber-based aerogels from wheat straw: influence of surface load and lignin content on their properties and dye removal capacity. *Biomolecules* 12, 232. <https://doi.org/10.3390/biom12020232>.
- Perera, H.M., Rajapaksha, A.U., Liyanage, S., Eknanayake, A., Selvasambian, R., Daverey, A., Vithanage, M., 2023. Enhanced adsorptive removal of hexavalent chromium in aqueous media using chitosan-modified biochar: Synthesis, sorption mechanism, and reusability. *Environ. Res.* 231, 115982. <https://doi.org/10.1016/j.envres.2023.115982>.
- Qiu, Z., Gao, F., Zhang, Y., Li, J., You, Y., Lv, X., Dang, J., 2024. Advancing wastewater treatment and metal recovery: Aminated ZIF-8 composite cellulose aerogel as an innovative biomass adsorbent for enhanced molybdenum ion adsorption. *Sep. Purif. Technol.* 338, 126478. <https://doi.org/10.1016/j.seppur.2024.126478>.
- Qu, J., Zhang, X., Liu, S., Li, X., Wang, S., Feng, Z., Wu, Z., Wang, L., Jiang, Z., Zhang, Y., 2022. One-step preparation of Fe/N co-doped porous biochar for chromium(VI) and bisphenol A decontamination in water: insights to co-activation and adsorption mechanisms. *Bioresour. Technol.* 361, 127718. <https://doi.org/10.1016/j.biortech.2022.127718>.
- Qu, J., Che, N., Niu, G., Liu, L., Li, C., Liu, Y., 2023. Iron/manganese binary metal oxide-biochar nano-composites with high adsorption capacities of Cd²⁺: Preparation and adsorption mechanisms. *J. Water Process Eng.* 51, 103332. <https://doi.org/10.1016/j.jwpe.2022.103332>.
- Ramachandran, T., Hamed, F., Kumar, Y.A., Raji, R.K., Hegazy, H.H., 2023a. Multifunctional covalent-organic frameworks (COFs)-2D MXenes composites for diverse applications. *J. Energy Storage* 73, 109299. <https://doi.org/10.1016/j.est.2023.109299>.
- Ramachandran, T., Hamed, F., Raji, R.K., Majhi, S.M., Barik, D., Kumar, Y.A., Jauhar, R. M., Pachamuthu, M.P., Vijayalakshmi, L., Ansar, S., 2023b. Enhancing asymmetric supercapacitor performance with NiCo₂O₄-NiO hybrid electrode fabrication. *J. Phys. Chem. Solids* 180, 111467. <https://doi.org/10.1016/j.jpccs.2023.111467>.
- Ramachandran, T., Sana, S.S., Kumar, K.D., Kumar, Y.A., Hegazy, H.H., Kim, S.C., 2023c. Asymmetric supercapacitors: Unlocking the energy storage revolution. *J. Energy Storage* 73, 109096. <https://doi.org/10.1016/j.est.2023.109096>.
- Saleem, S., Animasau, I.L., Yook, S.J., Al-Mdallal, Q.M., Shah, N.A., Faisal, M., 2022. Insight into the motion of water conveying three kinds of nanoparticles shapes on a horizontal surface: Significance of thermo-migration and Brownian motion. *Surf. Interfaces* 30, 101854. <https://doi.org/10.1016/j.surfint.2022.101854>.
- Shen, Y., Fu, F., Tang, B., 2023. Ethylenediamine-functionalized MnFe₂O₄@ferrihydrite as a magnetic adsorbent for removal of Cr(VI): Adsorption and mechanism studies. *J. Environ. Chem. Eng.* 11, 110230. <https://doi.org/10.1016/j.jece.2023.110230>.
- Su, L., Zhang, H., Oh, K., Liu, N., Luo, Y., Cheng, H., Zhang, G., He, X., 2021. Activated biochar derived from spent Auricularia auricula substrate for the efficient adsorption of cationic azo dyes from single and binary adsorptive systems. *Water Sci. Technol.* 84, 101–121. <https://doi.org/10.2166/wst.2021.222>.
- Sun, Y., Wang, T., Han, C., Bai, L., Sun, X., 2023. One-step preparation of lignin-based magnetic biochar as bifunctional material for the efficient removal of Cr(VI) and Congo red: Performance and practical application. *Bioresour. Technol.* 369, 128373. <https://doi.org/10.1016/j.biortech.2022.128373>.
- Teng, L., Yue, C., Zhang, G., 2023. Epoxied SiO₂ nanoparticles and polyethyleneimine (PEI) coated polyvinylidene fluoride (PVDF) membrane for improved oil water separation, anti-fouling, dye and heavy metal ions removal capabilities. *J. Colloid Interface Sci.* 630, 416–429. <https://doi.org/10.1016/j.jcis.2022.09.148>.
- Wan, Y., Luo, H., Cai, Y., Dang, Z., Yin, H., 2023. Selective removal of total Cr from a complex water matrix by chitosan and biochar modified-FeS: Kinetics and underlying mechanisms. *J. Hazard. Mater.* 454, 131475. <https://doi.org/10.1016/j.jhazmat.2023.131475>.
- Wang, F., Animasau, I.L., Al-Mdallal, Q.M., Saranya, S., Muhammad, T., 2023b. Dynamics through three-inlets of t-shaped ducts: Significance of inlet velocity on transient air and water experiencing cold fronts subject to turbulence. *Int. Commun. Heat. Mass.* 148, 107034. <https://doi.org/10.1016/j.icheatmasstransfer.2023.107034>.
- Wang, J., Guo, X., 2020. Adsorption isotherm models: Classification, physical meaning, application and solving method. *Chemosphere* 258, 127279. <https://doi.org/10.1016/j.chemosphere.2020.127279>.
- Wang, B., Lan, J., Bo, C., Gong, B., Ou, J., 2023a. Adsorption of heavy metal onto biomass-derived activated carbon: review. *RSC Adv.* 13, 4275–4302. <https://doi.org/10.1039/d2ra07911a>.
- Wang, H., Shan, L., Lv, Q., Cai, S., Quan, G., Yan, J., 2020. Production of hierarchically porous carbon from natural biomass waste for efficient organic contaminants adsorption. *J. Clean. Prod.* 263, 121352. <https://doi.org/10.1016/j.jclepro.2020.121352>.
- Wang, Q., Shao, J., Shen, L., Xiu, J., Shan, S., Ma, K., 2022. Pretreatment of straw using filamentous fungi improves the remediation effect of straw biochar on bivalent cadmium contaminated soil. *Environ. Sci. Pollut. Res.* 29, 60933–60944. <https://doi.org/10.1007/s11356-022-20177-2>.
- Wang, T., Sun, Y., Bai, L., Han, C., Sun, X., 2023d. Ultrafast removal of Cr(VI) by chitosan coated biochar-supported nano zero-valent iron aerogel from aqueous solution: Application performance and reaction mechanism. *Sep. Purif. Technol.* 306, 122631. <https://doi.org/10.1016/j.seppur.2022.122631>.
- Wang, K., Zhang, F., Xu, K., Che, Y., Qi, M., Song, C., 2023c. Modified magnetic chitosan materials for heavy metal adsorption: a review. *RSC Adv.* 13, 6713–6736. <https://doi.org/10.1039/d2ra07112f>.
- Wu, Z., Zhao, C., Zeng, W., Wang, X., Liu, C., Yu, Z., Zhang, J., Qiu, Z., 2022. Ultra-high selective removal of Cr and Cr(VI) from aqueous solutions using polyethyleneimine functionalized magnetic hydrochar: Application strategy and mechanisms insight. *Chem. Eng. J.* 448, 137464. <https://doi.org/10.1016/j.cej.2022.137464>.
- Xiao, F., Cheng, J., Cao, W., Yang, C., Chen, J., Luo, Z., 2019. Removal of heavy metals from aqueous solution using chitosan-combined magnetic biochars. *J. Colloid Interface Sci.* 540, 579–584. <https://doi.org/10.1016/j.jcis.2019.01.068>.
- Xu, Y., Chen, J., Chen, R., Yu, P., Guo, S., Wang, X., 2019. Adsorption and reduction of chromium(VI) from aqueous solution using polypyrrole/calcium rectorite composite adsorbent. *Water Res.* 160, 148–157. <https://doi.org/10.1016/j.watres.2019.05.055>.
- Yang, Q., Wu, P., Liu, J., Rehman, S., Ahmed, Z., Ruan, B., Zhu, N., 2020. Batch interaction of emerging tetracycline contaminant with novel phosphoric acid activated corn straw porous carbon: Adsorption rate and nature of mechanism. *Environ. Res.* 181, 108899. <https://doi.org/10.1016/j.envres.2019.108899>.
- Yang, Y., Zhang, Y., Wang, G., Yang, Z., Xian, J., Yang, Y., Li, T., Pu, Y., Jia, Y., Li, Y., Cheng, Z., Zhang, S., Xu, X., 2021. Adsorption and reduction of Cr(VI) by a novel nanoscale FeS/chitosan/biochar composite from aqueous solution. *J. Environ. Chem. Eng.* 9, 105407. <https://doi.org/10.1016/j.jece.2021.105407>.
- Yedluri, A.K., Kim, H.-J., 2018. Wearable super-high specific performance supercapacitors using a honeycomb with folded silk-like composite of NiCo₂O₄ nanoplates decorated with NiMoO₄ honeycombs on nickel foam. *Dalton Trans.* 47, 15545–15554. <https://doi.org/10.1039/C8DT03598A>.
- Yedluri, A.K., Kim, H.J., 2019. Enhanced electrochemical performance of nanoplate nickel cobaltite (NiCo₂O₄) supercapacitor applications. *RSC Adv.* 9, 1115–1122. <https://doi.org/10.1039/c8ra09081e>.
- Yuan, X., Li, J., Luo, L., Zhong, Z., Xie, X., 2023. Advances in sorptive removal of hexavalent chromium (Cr(VI)) in aqueous solutions using polymeric materials. *Polymers (Basel)* 15, 388. <https://doi.org/10.3390/polym15020388>.
- Zang, X., Jiang, R., Zhu, H.Y., Wang, Q., Fu, Y.Q., Zhao, D.X., Li, J.B., Liu, H., 2024. A review on the progress of magnetic chitosan-based materials in water purification and solid-phase extraction of contaminants. *Sep. Purif. Technol.* 454, 125521. <https://doi.org/10.1016/j.seppur.2023.125521>.
- Zhang, M.M., Liu, Y.G., Li, T.T., Xu, W.H., Zheng, B.H., Tan, X.F., Wang, H., Guo, Y.M., Guo, F.Y., Wang, S.F., 2015. Chitosan modification of magnetic biochar produced from *Eichhornia crassipes* for enhanced sorption of Cr(VI) from aqueous solution. *RSC Adv.* 5, 46955–46964. <https://doi.org/10.1039/c5ra02388b>.

- Zhang, X., Tian, J., Wang, P., Liu, T., Ahmad, M., Zhang, T., Guo, J., Xiao, H., Song, J., 2022a. Highly-efficient nitrogen self-doped biochar for versatile dyes' removal prepared from soybean cake via a simple dual-templating approach and associated thermodynamics. *J. Clean. Prod.* 332, 130069 <https://doi.org/10.1016/j.jclepro.2021.130069>.
- Zhang, H., Xiao, R., Li, R., Ali, A., Chen, A., Zhang, Z., 2020. Enhanced aqueous Cr(VI) removal using chitosan-modified magnetic biochars derived from bamboo residues. *Chemosphere* 261, 127694. <https://doi.org/10.1016/j.chemosphere.2020.127694>.
- Zhang, Y., Zhao, S., Mu, M., Wang, L., Fan, Y., Liu, X., 2022b. Eco-friendly ferrocene-functionalized chitosan aerogel for efficient dye degradation and phosphate adsorption from wastewater. *Chem. Eng. J.* 439, 135605 <https://doi.org/10.1016/j.cej.2022.135605>.
- Zhao, Y., Shi, H., Du, Z., Zhou, J., Yang, F., 2023. Removal of As(V) from aqueous solution using modified Fe₃O₄ nanoparticles. *R Soc. Open Sci.* 10, 220988 <https://doi.org/10.1098/rsos.220988>.
- Zhao, B., Tang, J., Lyu, H., Liu, F., Wang, L., 2022. Low molecular weight organic acids strengthen the electron transfer of natural FeS₂/biochar composite for Cr(VI) reduction: experimental observations and governing mechanisms. *J. Environ. Chem. Eng.* 10, 107181 <https://doi.org/10.1016/j.jece.2022.107181>.
- Zhao, J., Yang, X., Liang, G., Wang, Z., Li, S., Wang, Z., Xie, X., 2020. Effective removal of two fluoroquinolone antibiotics by PEG-4000 stabilized nanoscale zero-valent iron supported onto zeolite (PZ-NZVI). *Sci. Total Environ.* 710, 136289 <https://doi.org/10.1016/j.scitotenv.2019.136289>.
- Zhu, C., Huang, H., Chen, Y., 2022. Recent advances in biological removal of nitroaromatics from wastewater. *Environ. Pollut.* 307, 119570 <https://doi.org/10.1016/j.envpol.2022.119570>.
- Zoroufchi Benis, K., Sokhansanj, A., Hughes, K.A., McPhedran, K.N., Soltan, J., 2023. An engineered biochar for treatment of selenite contaminated water: Mass transfer characteristics in fixed bed adsorption. *Chem. Eng. J.* 469, 143946 <https://doi.org/10.1016/j.cej.2023.143946>.